Fractographic analysis of tensile failure of acrylonitrile-butadiene-styrene fabricated by fused deposition modeling

Jaret C. Riddick*, Mulugeta A. Haile, Ray Von Wahlde, Daniel P. Cole, Oluwakayode Bamiduro, Terrence E. Johnson

Vehicle Technology Directorate, US Army Research Lab, Aberdeen Proving Ground, MD 21005, United States

ARTICLE INFO

ABSTRACT

The aim of the present study is to utilize fractographic methods employing scanning electron microscope (SEM) images to investigate the effects of build direction and orientation on the mechanical response and failure mechanism for Acrylonitrile–Butadiene–Styrene (ABS) specimens fabricated by fused deposited modeling (FDM). The material characterized here is ABS-M30 manufactured by Stratasys, Inc. Measurements of tensile strength, elongation-at-break and tensile modulus measurements along with the failure surfaces were characterized on a range of specimens at different build direction and raster orientation: $\pm45°$, $0°$, $0/90°$, and $90°$. The analysis of mechanical testing of the tensile specimens until failure will contribute to advances in creating stronger and more robust structure for various applications. Parameters, such as build direction and raster orientation, can be interdependent and exhibit varying effects on the properties of the ABS specimens. The ABS-M30 specimens were found to exhibit anisotropy in the mechanical response when exposed to axial tensile loading. The stress-strain data was characterized by a monotonic increase with an abrupt failure signifying brittle fracture. In certain combinations of build direction and raster orientation tensile failure was preceded by slight softening. The tensile strength and modulus, and elongation-at-break were found to be highly dependent upon the raster orientation and build direction. The relationship between the mechanical properties and failure was established by fractographic analysis. The fractographic analysis offers insight and provides valuable experimental data for the purpose of building structures in orientations tailored to their exemplified strength. For instance, specimens loaded such that bonds between adjacent rasters are the primary load bearing mechanism offer the least significant failure resistance. Other examples are shown where artifacts of the FDM fabrication process act to enhance tensile strength when configured properly with respect to the load. The results highlighted in this study are fundamental to the development of optimal design of complex ultra-light structure weight with increased structural efficiency. The study also presents a systematic scheme employing analogs to traditional fiber-reinforced polymer composites for the designation of build orientation and raster orientation parameters.

© 2016 Elsevier B.V. All rights reserved.

1. Introduction

Additive manufacturing (AM) is a design solution based upon computer-aided design (CAD) and computer-aided manufacturing (CAM) that enables the rapid production of three-dimensional (3D) solid prototypes from a computer file. AM, sometimes referred to as direct digital manufacturing (DDM), or generically as 3D printing, employs advanced technology to optimize development of complex parts and molds with unique surface topologies by reducing time and labor cost by eliminating the need for substantial, and costly, tooling. Commercially available AM techniques include direct metal laser sintering (DMLS), ultrasonic additive manufacturing (UAM), electron beam melting (EBM), and fused deposition modeling (FDM) [1].

Recent trends indicate that AM technologies have the potential to become ubiquitous and democratize access to manufacturing [2].
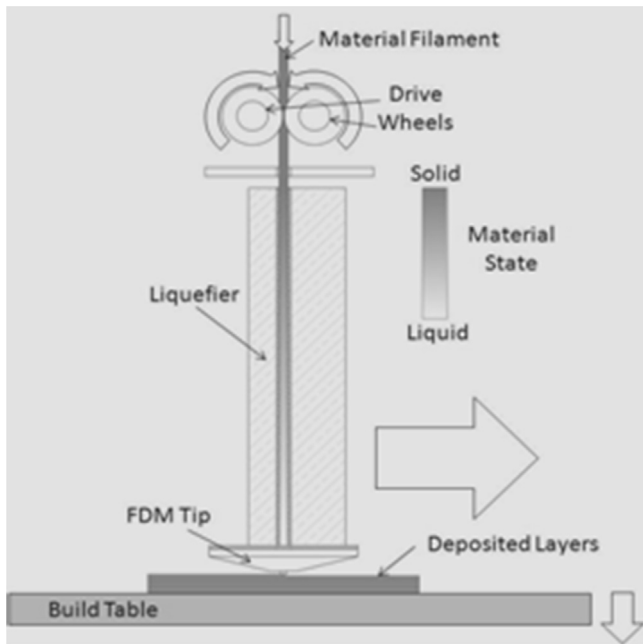
Fig. 1. Fused deposition modeling (FDM) process.

Fig. 2. Horizontal build direction (For interpretation of the references to color in the text, the reader is referred to the web version of this article).

Fig. 3. Side build direction (For interpretation of the references to color in the text, the reader is referred to the web version of this article).

Moreover, the flexibility of sharing designs offers the advantage of working with different materials to create an array structures of desired properties. For instance, 3D printing exemplifies its usability in areas such as designing and fabricating scaffolds for tissue engineering [3], dental models [4], elastomeric seals and bushings [5], dense structural ceramic and metallic components by sintering of polymer bound "green" ceramic/metallic parts [6] and custom prosthesis and implants [7], novel and energy absorbing structural configurations [8,9].

The present study is an experimental investigation of the effect of selected manufacturing parameters on the mechanical properties and ultimate failure of specimens fabricated by FDM, utilizing scanning electron microscope (SEM) images, referred to as fractographs. For the present study, FDM was chosen due to its rapid growth as a method-of-choice among a wide variety of users [2]. Developed by Stratasys® Inc. in 1990, FDM accomplishes 3D printing by depositing thermoplastic material layer-by-layer. The modeling process is initiated by creating a graphical model using sophisticated 3D CAD software. The file containing the CAD model is then converted into 3D stereolithography (STL) format. The STL file data is used to tessellate the model of the part into cross-sectional facets upon which tool paths can be projected for forming each layer [10]. FDM processing is carried out by forcing a filament composed of thermoplastic material, referred to as feedstock, into a liquefier where it is softened to a molten state to be delivered through a nozzle under pressure for deposition onto a platform stage (Fig. 1). The material solidifies quickly due to cooling by the surrounding colder air. Subsequent layers are joined as molten material is deposited on solidified material to form layers and eventually build up a part. Several feedstock materials are widely used such as acrylonitrile–butadiene–styrene (ABS), polyphenylsulfone (PPSF), polycarbonate, and polyetherimide (PEI), known as Ultem® 9085. FDM processing has also been adapted to produce composite materials, such as short-fiber reinforced polymers [11] and carbon-nanotube reinforced ABS [12] and ceramics [13]. Ceramic materials have also been used in FDM to produce piezoceramic composite materials [14] and polymer-ceramic composites [15,16]. Experimental methods have been proposed to use AM to produce fu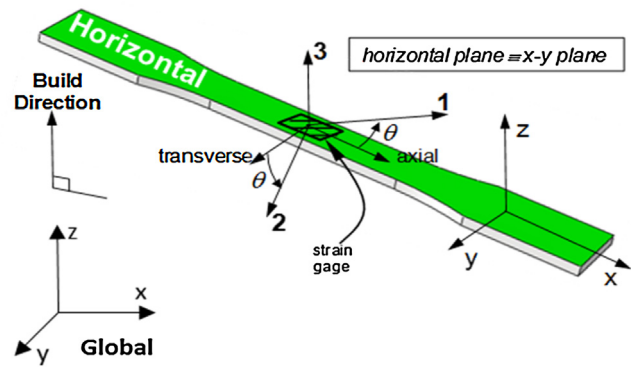nctional structural components by either hybrids of existing processes or by new approaches to fabricate functional composite structures [17,18].

The material subject of investigation in this work is a thermoplastic and a copolymer, ABS-M30 manufactured by Stratasys, Inc. The ABS-M30 is classified also as a glassy polymer for temperature below its glass transition temperature (T_g = 105 °C). The resulting material combines the strength and rigidity of styrene and acrylonitrile polymers with the toughness of polybutadiene rubber. By varying proportions of the three constituents, various modifications can be made to improve impact resistance, toughness, heat resistance, and chemical resistance. Rapid prototyped ABS presently enjoys wide use as a structural material in a variety of platforms. However, due to the proprietary nature of ABS material blends, mechanical properties reported in the literature vary widely creating a design hurdle.

Prior experimental studies of FDM have considered the special case of uni-axially-loaded, uni-directional specimens [19]. In at least one case, models have been developed to predict anisotropic behavior using uni-directional experimental data [5]. In other reports, studies have been reported the effect of porosity on mechanical properties via compressive testing [20] and the effects of layer orientation on mechanical properties of a polymer via three point bend testing [21]. The objective of the present study was to employ fractographic analysis to characterize the mechanical properties of tensile specimens constructed of ABS-M30 material fabricated by FDM using a Stratasys® Fortus 400 3D production system, and observe the effect of manufacturing parameters on failure, uncovered by analyzing the fracture surface. Various manufacturing parameters have been shown to effect fabrication of components by FDM [19]. For instance, build direction affects other factors such as build time, surface quality, feature resolution, as

Fig. 4. Vertical build direction (For interpretation of the references to color in the text, the reader is referred to the web version of this article).

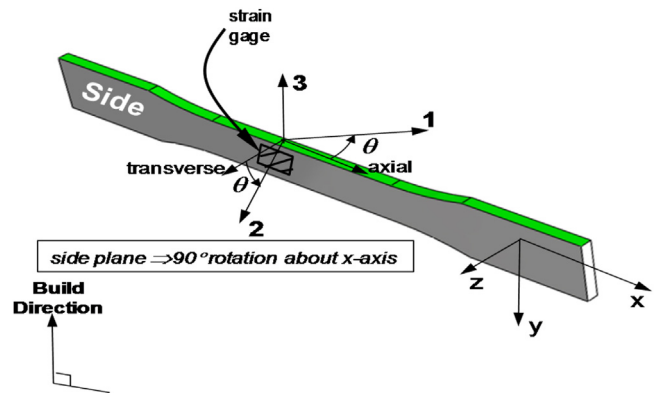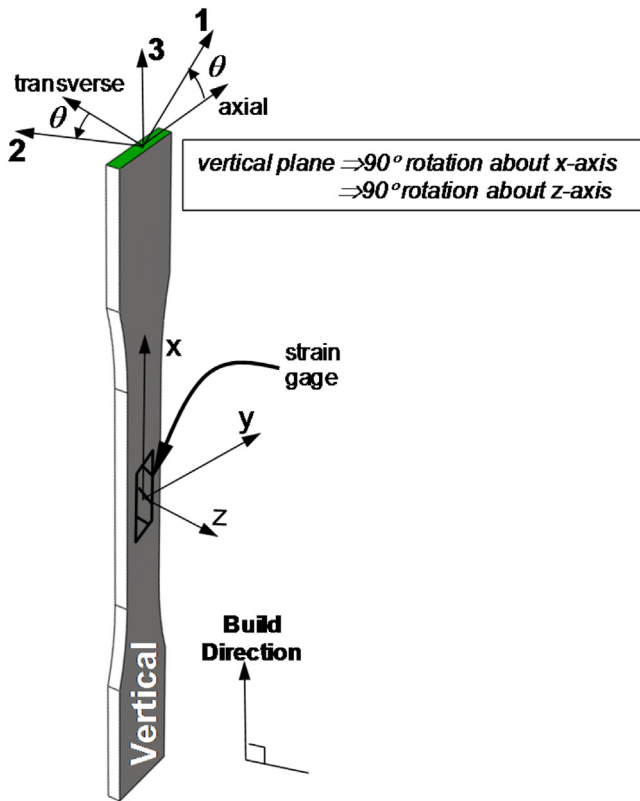**Fig. 5.** ASTM D638-08 tensile test specimen fabricated by FDM using ABS. (Overall length, 165 mm; test section length, 57 mm; test section width, 13 mm; specimen thickness, 3.5 mm).

well as the potential need for usage of sometimes complex support structure [22–24]. Moreover, the bead width, air gap, build temperature, color [19], raster width and layer thickness should be considered when executing a build via FDM [25]. The raster orientation defines the tool path in the plane of deposited layers (see Fig. 1). The manufacturing parameters were limited to build direction and raster orientation and specimens were loaded quasi-statically to failure. The report emphasizes a systematic naming convention for build directions, and utilizes a scheme borrowed from traditional fiber-reinforced composites to discuss the raster orientations [26]. The tensile test specimens were made using ABS-M30 filament according to ASTM D638-03, "Standard Test Method for Tensile Properties of Plastics." [27]. The results of the present study will be fundamental to the development of optimal designs of complex lightweight durable components where structural tailoring may offer an added benefit via weight reduction and structural efficiency. While past studies have presented test data, here the specimen response is considered with regard to consequences of design for structural performance in complex geometries.

2. Experiment

2.1. Specimen description

The FDM processing method is depicted in Fig. 1. The ABS-M30 feedstock filament material melts inside the liquefier at 204 °F, and is extruded out of the nozzle. Note, the color change in the liquefier section depicts the transition of the ABS filament form solid to a molten state. Volumetric error leading to high void density has been shown to degrade the desired structural properties in FDM processed parts [5,19]. In order to avoid volumetric error, a strategy of filling in the slice areas with the most material possible and minimizing gaps was chosen [28]. For each layer the outer shape
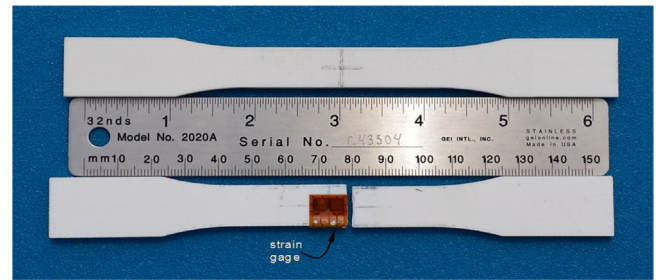
was traced with the specimen contour. The ideal nature of the raster orientation in the test section allowed the tool path optimization to be done manually using the INSIGHT CAM software, in lieu of a formalized contours approach [29,30]. A T10 tip size (see Fig. 1) was selected to yield the smallest slice height and bead width possible; 0.005″ and 0.008″ respectively.

Tensile test specimens were made using ABS-M30 according to ASTM D638-03. In each specimen, the raster orientation defines the tool path in the plane of the build in terms of the angle θ formed between the raster and the global x-axis, as depicted in Figs. 2–4. For each of the horizontal (H), side (S), and vertical (V) builds, the raster material axes, designated as the 1–3 axes in Figs. 2–4, are chosen to correspond to the build directions. Note that in all cases the material 3-axis coincides with the build direction. Each build direction has a different number of layers and volumetric errors. For the present investigation, the three different build directions were tested and their respective failure responses due to tensile load were compared. Fig. 2 shows the H build direction. Note that the specimen definitions relate directly to the traditional material definitions of composite materials, where the raster orientation 1- and 2-axes correspond to the global Cartesian X- and Y- axes [26], shown in Fig. 2. The build orientation, x-y-z, associated with each specimen build reflect rotations of the specimen about the global X-, Y-, Z- axes of Fig. 2. Fig. 3 shows the S build direction, where the raster orientation axes have been rotated 90° counter-clockwise (CCW) about the global X-axis. Finally, Fig. 4 shows the V build direction, where the raster orientation axes have been rotated 90° CCW about the about the global Z-axis, followed by a 90° CCW rotation about the global x-axis. This set of rotations constitutes a systematic scheme to designate build orientations. In all cases the orientation x-axes align as the tensile load direction for the specimens. Table 1 designates the 12 raster orientations for various specimens considered for the study.

2.2. Experimental set-up

A biaxial strain gage (Micro-Measurements CEA-06-125UT-350, 350 Ω General Purpose Strain Gage) was placed at the center of the specimen, as shown in the labels in Figs. 2–4, and on the failed specimen in Fig. 5. The ABS specimens were characterized according to the ASTM D638-03. The Instron 5565 Tensile Tester with a 5-kN load cell was used for all experiments. The tests were run at a speed of 1.27 mm/min (0.05 in/min). Axial and transverse strains were recorded via a StrainSmart® Data Acquisition System. The experimental setup was first calibrated by testing a standard aluminum specimen. Five specimens from each sample build were then loaded until failure. The nomenclature presented in Table 1 defines the twelve sample builds according to build directions and raster orientations, based upon the tool path on the planar surfaces associated with the material 1–2 planes in Figs. 2–4 (highlighted in green).
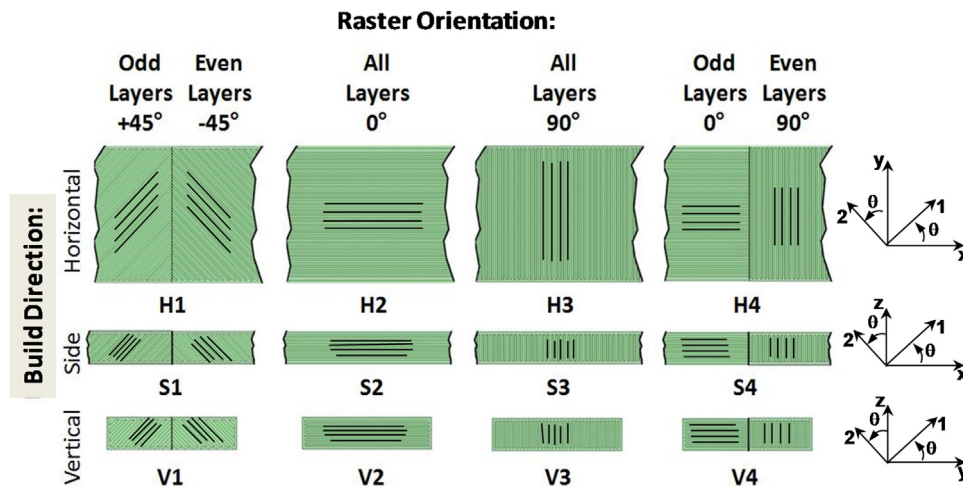
Raster Orientation:

Fig. 6. Build direction and raster orientation for each specimen type. Top view depicted, viewing downward along the axis associated with build direction, where x-axis is the loading direction (the material 3-axis).

Fig. 6 illustrates the raster profile in accordance with the build direction and the orientation angle with respect to the orientation x-y-z axes corresponding to the planes highlighted in green in Figs. 2–4. Samples H1, S1, and V1 correspond to horizontal, side, and vertical build directions, respectively, with ±45° raster orientation, where the odd layers are composed of $\theta = 45°$ rasters and the even layers are composed of $\theta = -45°$ rasters. Samples H2, S2, and V2 correspond to horizontal, side, and vertical build directions, respectively, with $\theta = 0°$ raster orientation, where all layers are composed of $\theta = 0°$ rasters. Samples H3, S3, and V3 correspond to horizontal, side, and vertical build directions, respectively, with 90° raster orientation, where all layers are composed of $\theta = 90°$ rasters. Finally, samples H4, S4, and V4 correspond to horizontal, side, and vertical build directions, respectively, with 0° and 90° raster orientation, where the odd layers are composed of $\theta = 0°$ rasters and the even layers are composed of $\theta = 90°$ rasters. The x-axes in the orientation coordinate systems depicted to the right of the specimen definitions in Fig. 6 correspond to the load axes for each build direction (Figs. 2–4). Note that for the vertical build direction the build orientation and x-axis coincide. Therefore, the vertical build direction and the load axis are the same. The specimen fails across the its width (Fig. 6) forming a fracture surface along the orientation y-axis, perpendicular to the loading direction (orientation x-axis) Microscopic images of the fracture surfaces resulting from tensile tests to failure (ASTM D638-03) were obtained using the Hitachi® TM1000 Tabletop Scanning Electron Microscope (SEM), and will be highlighted throughout.

Note that in certain cases, build directions and raster orientations combine to form cross sections normal to the plane of loading that appear identical in character. Here, these relationships will be utilized along with other observations to build conclusions about the failure response. Finally, the H1 sample displays characteristics analogous to a traditional ±45° fiber-reinforced composite laminate. Therefore, the shear modulus of the H1 sample will be approximated according to ASTM D3518, "Standard Test Method for In-Plane Shear Response of Polymer Matrix Composite Materials by Tensile Test of a ±45° Laminate [31]."

3. Results and discussion

Fig. 7 shows the stress-strain curves for the side (S, green), horizontal (H, red), and vertical (V, blue) build directions grouped by the raster orientations: ±45°, 0°, 90°, 0°/90°. The tensile strength, tensile modulus, elongation-at-break and Poisson's ratio are shown in Table 2 for each specimen designation, grouped by build direction and listed in order of descending average tensile strength. The standard deviation in each case indicates good agreement among the specimens tested for each sample designation. Primarily, the results indicate monotonically increasing stress-strain curves that conclude abruptly indicating a brittle fracture. In the case of one H2 specimen and all H1 specimens, the results in Fig. 7 indicate softening accompanied by some degree of necking before an abrupt failure. A similar softening is seen in the S3 orientation specimen. Considering the stress-strain results of Fig. 7, along with the results shown in Table 2, the S build direction specimens consistently display the highest average tensile strength and modulus for all raster orientations, where the values in descending order of magnitude correspond to raster orientations: 0°, ±45°, 0°/90°, and 90°. In general, the V build direction specimens display relatively low tensile strength, and relatively high modulus of elasticity values. The H3 and V2 specimens display very similar average tensile strength, while the H3 specimens have a higher average tensile modulus value. The H3 specimen displays the highest elongation-at-break of all specimens tested, indicating an increase in strain capability.

3.1. 0° orientation

Fractographic images (Fig. 8) of the fracture surfaces of H2 and S2 specimens, respectively, indicate that the cross-sections, perpendicular to the loading direction, are nearly identical in

Table 1
Specimen nomenclature.

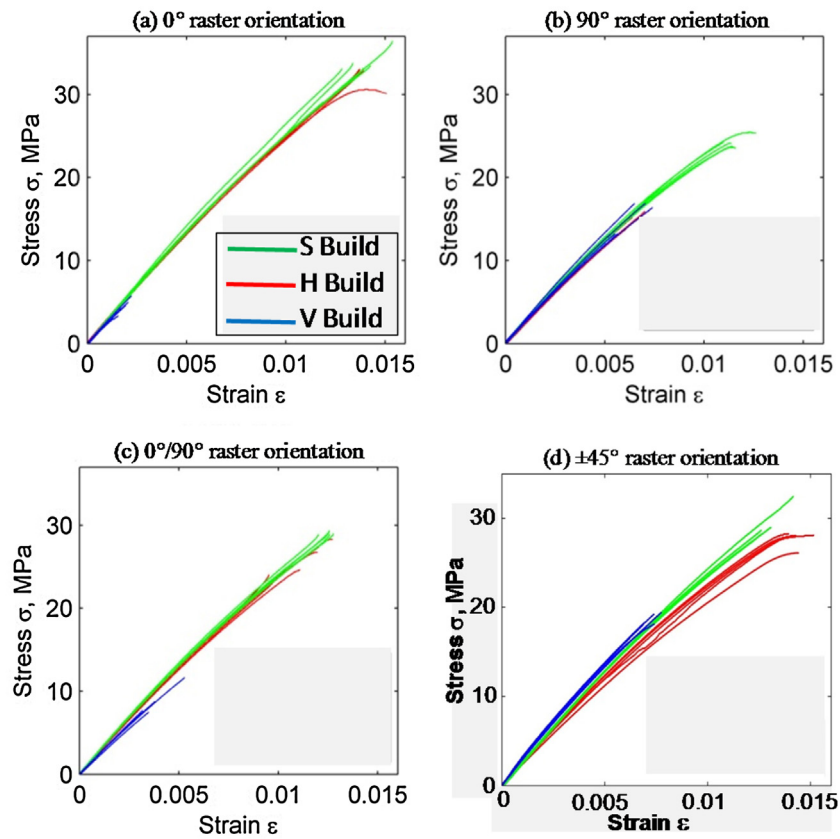| Build Directions	Raster Orientation			
	±45°	0°	90°	0°/90°
Horizontal	H1	H2	H3	H4
Side	S1	S2	S3	S4
Vertical	V1	V2	V3	V4

Fig. 7. Stress-strain results (For interpretation of the references to color in the text, the reader is referred to the web version of this article).
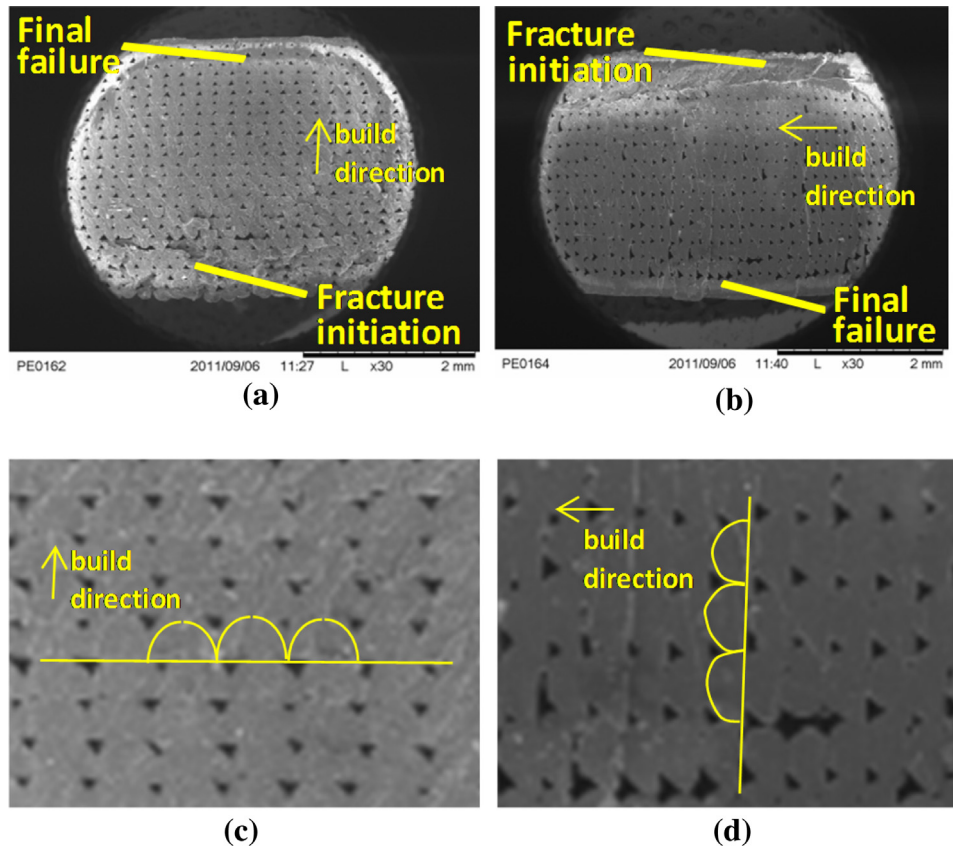

Fig. 8. 0° orientation specimen, (a) horizontal build, (b) side build, (c) zoom-in on horizontal build, and (d) zoom-in on side build.
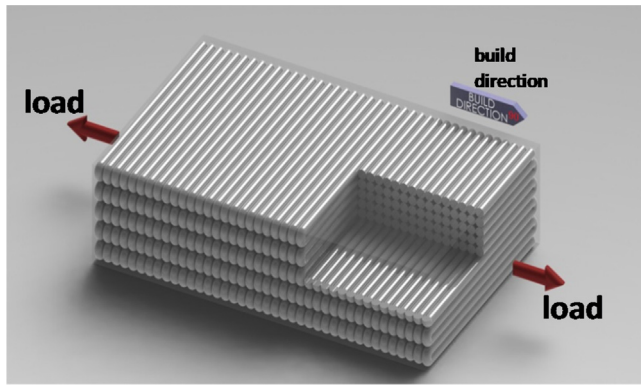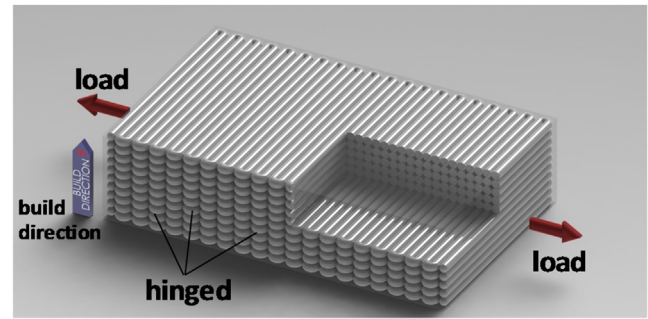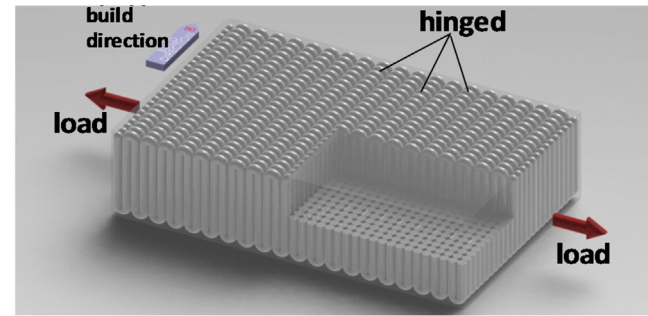
Fig. 9. Idealization of 0°orientation vertical build direction (V2).

(a) horizontal build direction (H3)

(b) side build direction (S3)

Fig. 10. Idealization of 90° orientation build directions.

appearance with respect to the orientation of the rasters. The nearly identical character of the cross sections imply that the structural response of the H2 and S2 specimens should be very similar. The tensile strength results in Table 2 indicate the average values for the H2 and S2 specimens are 32.5 and 34 MPa, respectively; a 4.5% difference. The average tensile modulus of the S2 specimen is 2.65 GPa, almost identical to the H2 specimen value of 2.6 GPa. Note in Fig. 8a and b, the failure initiates on the horizontal edge spanning the width along the orientation y-axis. of each specimen with breaking of individual raster cross-sections creating overload that allows the fracture to propagate across the fracture plane creating a clean surface up to "final failure." Because the load is carried along the raster axis, H2 and S2 specimens discussed here offer a unique comparison of effects present in the mechanical response of two specimens with like raster orientations fabricated in different build directions. Differences observed in the mechanical responses can be attributed to issues related to fabrication associated with build direction. Upon close inspection, the fractographs of Fig. 8c and d show that the rasters take on a semi-circular cross-section shape due to the stacking of layers. Semi-circular raster cross-sections stacked from bottom-to-top (build direction) in the H2 specimen, where the flat axis of each semi-circular raster cross-section is perpendicular to the build direction. The oval bead cross-sections stacked in the build direction for the S2 are oriented such the flat axis of each raster cross-section is in the through-thickness (z-axis) direction with respect to the loading axis (Fig. 3). The difference in the stacking of the raster cross-sections between the H2 and S2 specimens led to a rearrangement of the voids between the rasters, giving rise to the slight difference in the failure surfaces at the locations labeled "final failure," due to volumetric effects. The voids appear to be more closely packed in the S2 specimen. The area of

"fracture initiation" appears to be more densely packed and tightly fused in the S2 specimen, as opposed to the appearance of discreet failures of rasters and abundant voids in the "fracture initiation" location of the H2 specimen. Densely-packed, well-fused adjacent rasters at the fracture initiation site contribute to increased load bearing capacity, and therefore higher failure loads.

The V2 specimens present cross-section properties completely different from the H2 and S2 specimens. The average tensile strength of the V2 specimens is 15.14 MPa; 2.26 and 2.15 times less than the S2 and H2 specimens, respectively. Fig. 9 presents a graphical idealization of a section of vertical direction 0° orientation specimen (V2). According to the build direction shown in Fig. 9, the specimen is built up by stacking layers of material in the 1–2 material axis planes, where the 1-axis corresponds to the 0° material direction (Fig. 4). The red arrows in Fig. 9 indicate the loading direction. Note here that the rasters are applied in planes perpendicular to the load. The main load bearing mechanism here is adhesion between adjacent stacked cross-sections. The tensile failure creates a fracture plane between layers of rasters. Ultimately, the comparison amongst the 0° orientation specimens indicates

Table 2
ASTM D638 test results for ABS specimens fabricated by FDM (results are grouped according to specimen build direction and ranked by decreasing tensile strength within each grouping).

| Build Direction	Raster Orientation	Tensile Strength, MPa	Tensile Modulus, GPa	Elongation-at-Break, %	Poisson's ratio
Horizontal	0° (H2)	32.60 (1.11)[a]	2.69 (0.01)	1.40 (0.06)	0.38 (0.01)
	±45° (H1)	27.77 (0.92)	2.42 (0.10)	1.53 (0.05)	0.37 (0.00)
	0°/90° (H4)	25.69 (1.75)	2.59 (0.05)	1.11 (0.13)	0.37 (0.01)
	90° (H3)	15.26 (0.91)	2.45 (0.07)	0.58 (0.20)	0.36 (0.03)
Side	0° (S2)	34.17 (1.47)	2.79 (0.05)	1.40 (0.11)	0.38 (0.01)
	±45° (S1)	29.62 (1.96)	2.76 (0.03)	1.33 (0.06)	0.38 (0.01)
	0°/90° (S4)	29.11 (0.20)	2.65 (0.04)	1.27 (0.05)	0.37 (0.01)
	90° (S3)	24.24 (0.74)	2.53 (0.04)	1.16 (0.06)	0.36 (0.00)
Vertical	±45° (V1)	19.80 (2.22)	2.76 (0.03)	0.82 (0.17)	0.38 (0.01)
	0° (V2)	15.14 (1.99)	2.77 (0.13)	0.55 (0.07)	0.39 (0.01)
	0°/90° (V4)	13.61 (1.13)	2.74 (0.11)	0.50 (0.06)	0.38 (0.01)
	90° (V3)	12.42 (5.40)	2.67 (0.05)	0.48 (0.22)	0.38 (0.01)

[a] Standard deviation.
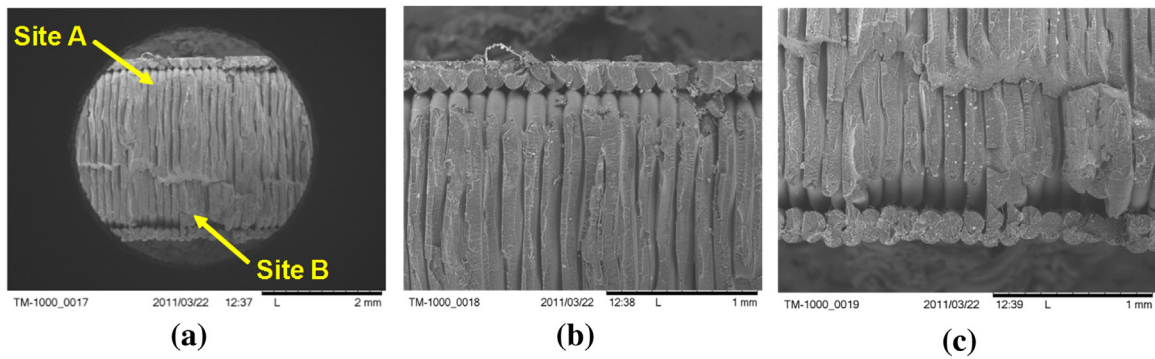
Fig. 11. Side build 90° orientation specimen (S3): (a) fracture surface, (b) enlargement of "Site A," and (c) enlargement of "Site B".
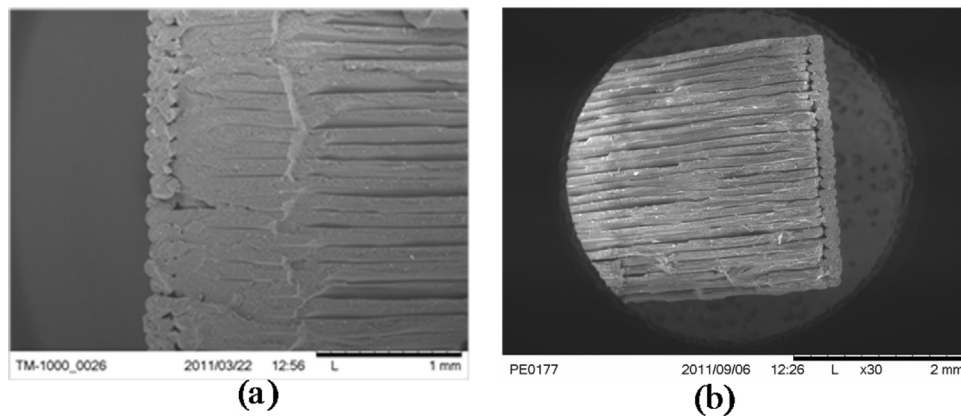

Fig. 12. Fracture surface of horizontal build 90° orientation specimen (H3): (a) left edge, broken hinge, (b) right edge, intact hinges.

bonds between rasters (V2), formed by applying molten material to hardened material layer-by-layer, exhibit a weaker load bearing capacity than the axially loaded rasters (H2 and S2). Furthermore, dense packing between adjacent rasters may result in fusing of rasters under loading, thereby improving the tensile response in materials composed of axially-loaded rasters.

3.2. 90° orientation

In the plane perpendicular to the load, the cross-sections of the H3, Fig. 10a, and V2, Fig. 9, specimens appear nearly identical with the exception of the boundaries. The average tensile strengths for the H3 and V2 specimens are 15.26 and 15.14 MPa, respectively. The S3 and V3 specimens also appear nearly identical in the plane perpendicular to the load. The S3 specimen displays the highest average tensile strength among the 90° build orientation specimens with a value of 22.24 MPa. The results for average tensile modulus of all 90° build orientation specimens indicate the moduli for the three build directions fall within the range of 2.32 and 2.44 GPa; a range of less than 5%. The average tensile strength for the V3 specimen is 15.30 MPa. Fig. 10 depicts the fashion in which the rasters are deposited for H3 and S3 specimens. Note that the pattern indicates that nozzle moves back-and-forth, in-plane, laying down material following a serpentine path to form the layers. The serpentine path of the horizontal build (H3) traverses back-and-forth along the 13-mm width of the specimen. For the S3 specimen the serpentine path traverses back-and-forth along the 3.5-mm thickness of the specimen. Therefore, for both the H3 and S3 specimens, the raster cross-sections normal to the load are hinged to one another, as shown in Fig. 10a and b.

In both the H3 and S3 specimens, the hinges between the layers are formed in the direction of the loading. Fig. 11a shows frac-tographs of the fracture surface of an S3 specimen. In Fig. 11b, raster surfaces forming the hinge from the fracture surface to the layer below are observed. Rough places on the fracture surface are an indication of the breaking of adhesion between layers. In Fig. 11c, there is evidence of tearing of rasters to expose the layer below the fracture surface leaving behind remnants of the hinge between the fracture surface and the layer above. A similar failure pattern can be observed in fractograph shown in Fig. 12 for the H3 specimen. In Fig. 12b, the rasters forming the hinge to the layer below the fracture surface are left smooth and intact, while Fig. 12a shows the tearing through of rasters exposing the layer below the fracture surface evidencing the hinge having been torn away. Evidence indicates that layers fail by initially forming failure surfaces between rasters in layers, after which the hinges act as reinforcement until the ultimate failure. Layers of the V3 specimen are formed by stacking layers in a fashion similar to the V2 specimen. The failure surface
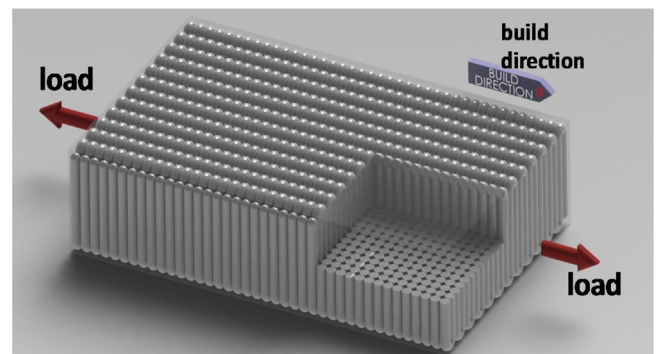

Fig. 13. Idealization of 90° orientation vertical build specimen (V3).
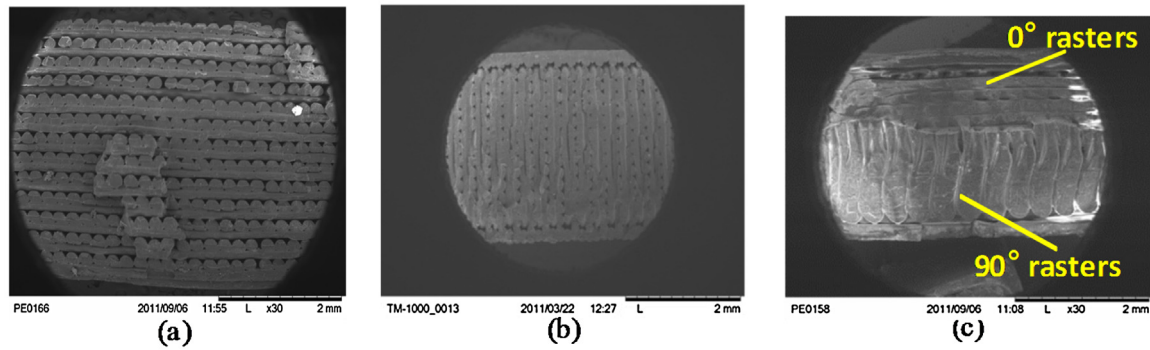
Fig. 14. Fracture surfaces for 0°/90° orientation specimens: (a) horizontal build (H4), (b) side build (S4), and (c) vertical build (V4).

of the V3 specimen (not shown here) indicated failure by separation of adjacent layers. No indication of tearing through of rasters was apparent. Therefore, it can be concluded that the failure load of the V3 specimen is a measure of the adhesion strength between layers normal to the load. Furthermore, the V2 specimen has a higher failure load than V3 specimen indicating a stronger adhesion between adjacent layers with longer rasters (i.e., spanning the 13 mm width dimension rather than the 3.5 mm thickness).

The S3, Fig. 10b, and V3, Fig. 13, have nearly identical cross-sections in the plane perpendicular to the load. However, the average tensile strength of the S3 (24.24 MPa) is nearly two times the value of the V3 (12.42 MPa) specimen. The strength results combined with the fractographic analysis indicate that the hinges between layers formed by the serpentine fashion in which material is deposited in-plane form reinforcements in the S3 specimens that significantly enhance strength.

The hinge reinforcement evidenced in H3 and S3 specimens can be considered a boundary effect. While both the H3 and S3 specimens have hinges between layers that act as reinforcement, the average strength of the S3 specimen (24.24 MPa) is just over 1.5 times greater than the value for the H3 (15.14 MPa) specimens. Noting Fig. 10, with respect to the cross-section normal to the load, the H3 specimen has its hinges stacked along the shorter cross-section dimension (thickness, 3.5 mm), while in the S3 specimen, the hinges are stacked along the longer dimension (width, 13 mm). The result is that there are significantly more hinge reinforcements in the S3 specimen than the H3 specimen. While the cross-sections of the H3 and V2 specimens are nearly identical with respect to the normal of load, the cross-sections of the H3 specimens are hinged to one another (Fig. 11) and the V2 cross-sections are not (Fig. 9). The average tensile strength of the H3 specimens is nearly 3.5 times that of the V2 specimens. Therefore the cross-section of the S3 specimen is dominated by the boundary effect due to axially-loaded raster material comprising the hinges, resulting in a higher tensile strength of S3 versus the H3 specimen.
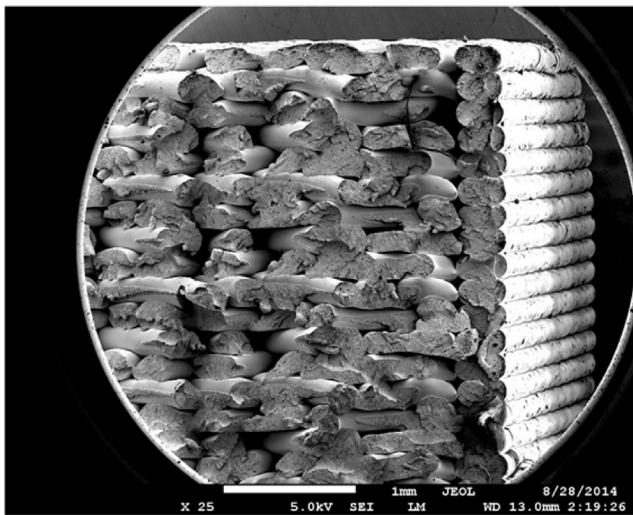
3.3. 0°/90° orientation

Consider the experimental results for the specimens with 0°/90° raster orientations in Table 2, namely H4, S4, and V4. For the S4 and V4 specimens, respectively, the tensile strength is nearly the average of the 0° (S2 and V2, respectively) and 90° (S3 and V3, respectively) raster orientation specimens, implying a sort of rule-of-mixtures type behavior with regards to average tensile strength. The fractograph in Fig. 14b shows a near equal distribution of 0° and 90° rasters in the cross-section of the S4 specimen. The micrograph in Fig. 14c shows tearing away of the 90° raster layer exposing the 0° layer below. The average tensile strength value for the H4 specimen is just over the average of the tensile strengths of the 0° H2 and 90° H3 specimens, indicating a deviation from rule-of-mixtures

type behavior. Evidence of broken 90° rasters in the fractograph of the H4 specimen in Fig. 14a indicates that the hinge reinforcement is not fully activated, and may indicate that other mechanisms are dominating the response The rule-of-mixtures behavior in the S4 specimen coupled with the clean break indicated by the fractograph of Fig. 14b indicates that the hinge reinforcement remains prominent in the response. The rule-of-mixtures behavior in the tensile strength response of the V4 specimens indicates that the mechanism identified in the V3 specimens (weaker adhesion between adjacent raster in layers with shorter rasters) is overcome by the inclusion of layers with longer (width-wise) rasters.
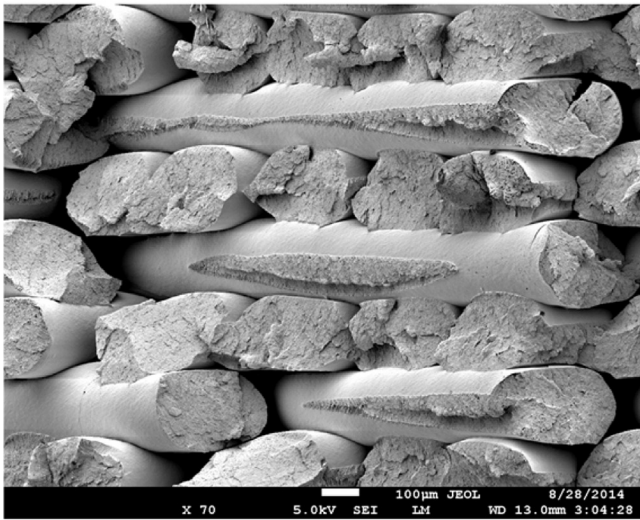
3.4. ±45° orientation

Idealizations of the ±45° raster orientations for each build direction are shown in Fig. 16. The tensile strengths of the H1, S1, and V1 specimens are 27.77 MPa, 29.62 MPa, and 19.80 MPa, respectively. The fractographs in Fig. 15 show the fracture surface in the H1 specimen. While the S1 specimens display higher tensile strength, the H1 specimens display a greater elongation-at-break, indicating more toughness. For H1 specimens, the pattern in the material axis 1–2 plane (see Fig. 4) forms an analog to ±45° fiber-feinforced composites (Jones, 1984). Therefore, as an approximation, the shear modulus of the H1 specimen was calculated using ASTM D3518, "Standard Test Method for In-Plane Shear Response of Polymer Matrix Composite Materials by Tensile Test of a ±45° Laminate." The method prescribed in the standard requires the shear modulus to be calculated by finding the quotient of the in-plane stress and the difference of the in-plane and transverse strains, measured by the bi-axial strain gage. The average shear modulus value for H1 specimens calculated per the standard is 885 MPa. By comparison, the well known shear modulus relationship for isotropic materials is given by $G = E/2(1 + v)$, where G is the shear modulus, E in the Young's modulus and v is the Poisson's ratio. Applying the values for tensile modulus and Poisson's ratio from Table 2 for the H1 specimen, the shear modulus derived from the isotropic assumption is 883 MPa. While the isotropic assumption cannot be applied to the H1 specimen, the calculations show that the present assumption provides an adequate estimate of the shear modulus.

For the H1 specimens, the rasters from ±45° angles with the load in the material 1–2 axis. Similar to the ±45° fiber-reinforced lamina in polymer composites, a buildup of load perpendicular to the rasters accounts for softening as the load increases to failure in the H1 specimens. The tensile response of the S1 specimens in Fig. 6 shows no softening and display a brittle-type failure load at a higher tensile load than the H1 specimens. A similar buildup of load perpendicular to the rasters within layers of the S1 specimen is overcome by edge effects. Note that the layers in the build direction of the S1 specimen, shown in Fig. 16b, consist of hinges that confine the area allowed for buildup of loads and exaggerate the
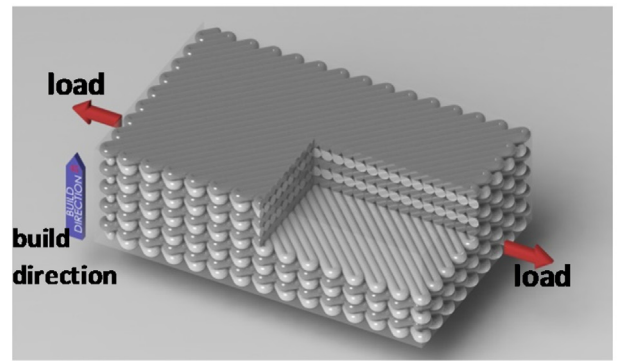
Fig. 15. Horizontal (H1) ±45° orientation specimen, (a) fracture surface, (b) enlarged view.

Fig. 16. Idealization of ±45° orientation build directions.

edge effects. The overall effect of the configuration of the S1 specimen is an increase in tensile strength versus the H1 specimen due in large part to the hinges and the interaction of the edge effects.
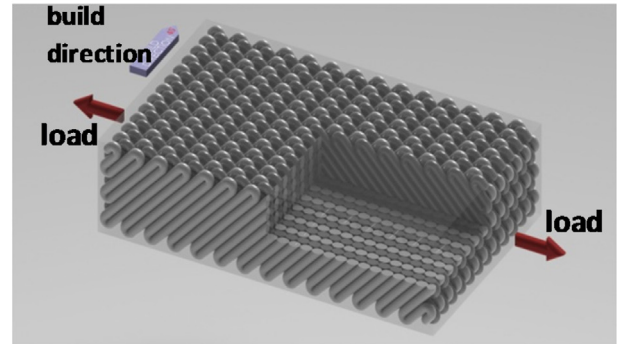
Finally, the V1 specimens exhibit the highest tensile strength values among the vertical build specimens. Inspection of the fracture surfaces of the V1 specimens reveals no apparent indicia of the cause for increased tensile strength among the vertical build specimens. Noting that the stress strain curves for the V1 specimens in Fig. 7 signify slight indications of softening before failure. There may be some buildup of load perpendicular to the rasters in the material 1–2 axis as seen in the H1 specimen. This may provide a toughening mechanism leading the leading to an increase in failure strength for the V1 specimens.
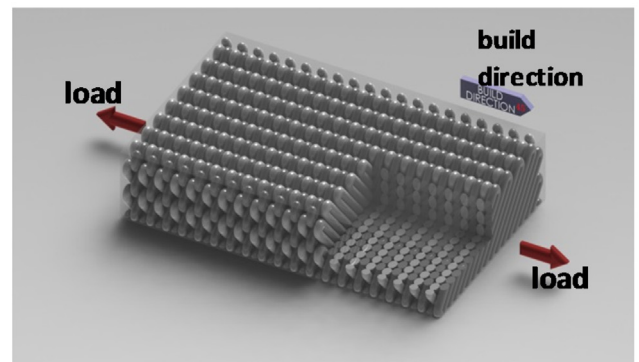
4. Conclusion

Specimens of ABS material fabricated by FDM technique were tested in uniaxial tension in accordance with ASTM Standard D638-03 to assess the effect of selected manufacturing parameters on tensile failure response. As defined by a systematic set of rotations about a fixed global Cartesian *x-y-z* axis, build directions were

varied between horizontal, side, and vertical directions. In general, raster orientations were varied between ±45°, 0°, 90°, and 0°/90°, in the layer of deposition. The stress-strain results of the tensile tests were characterized by a monotonic increase with an abrupt failure signifying brittle fracture. The stress-strain response of the ±45° horizontal specimen was characterized by evident softening due to the shear response, resulting in the greatest elongation-at-break value of all the specimens tested. The tensile modulus ranged from 2.45 GPa for the 90° horizontal build specimen to 2.79 GPa for the 0° side build specimen. Tensile strength ranged from 12.42 MPa for the 0° vertical build to 34.17 MPa for the 0° side build specimen.

In the case of the 0° horizontal and side build specimens, while the cross-sections appear almost exactly similar, and the stiffness are 2.6 GPa and 2.65 GPa, respectively, and the ultimate strengths are 32.6 MPa and 34.17 MPa. Fractographic analysis reveals that the side build specimens make better use of the geometry of the raster to fill the voids between rows. Therefore, the side build specimens benefit from lower volumetric error, and the effect is seen in

the resistance to failure. The horizontal build ±45° raster orientation specimens displayed softening prior to failure and the greatest elongation-at-break due to the effects of shear. An analog to ±45° composite laminates was applied to calculate the shear modulus of the horizontal build ±45° raster orientation specimen. A comparison showed the isotropic formulation of shear modulus to be an adequate estimate of shear modulus value for the horizontal build ±45° raster orientation specimens. The tensile response of the side build ±45° raster orientation specimens are not prone to the softening and display a brittle-type failure load at a higher tensile load than the horizontal build ±45° raster orientation specimens. The softening displayed by the horizontal build specimens can be attributed to a buildup of loads perpendicular to the rasters within the layers, while the side build ±45° raster orientation specimens are stronger due in large part to edge effects dominated by the existence of hinges.

The mechanisms for load bearing greatly influenced the resulting failure. In certain cases, vastly different combinations of build direction and raster orientation produced cross-sections characterized by similar raster orientation with the respect to the normal direction of the applied load. The resulting response for such similar cross-sections was seen to vary drastically. For example, the side build 90° raster orientation specimens and the vertical build 90° raster orientation specimens share similar cross-sections but the average tensile stiffness values are 2.53 GPa and 2.45 GPa, respectively; while the average tensile strengths are 24.24 MPa and 12.42 MPa, respectively. The vertical build 90° specimen is formed by stacking cross-sections in the loading direction. Adhesion between rasters in successive layers are the main load bearing mechanism. The side build 90° specimen is formed by laying rasters in a serpentine fashion within the layer of deposition, thereby forming hinges between the cross-sections normal to the load. The hinges act as reinforcement in the direction of the load to enhance tensile strength; the hinge reinforcement must be overcome to fail the specimen. Hence, a seeming artifact of the construction has a major impact on the ultimate mechanical performance of the specimen.

In another example of the effect of the hinge reinforcement, the horizontal build 90° specimen and the vertical build 0° share the same cross section and nearly identical tensile strength at 15.26 and 15.14 MPa, respectively. While the 90° horizontal build specimen does have hinge reinforcement, its volume is dominated by adjacent bonded rasters as the primary load bearing, thus cancelling the effect of the hinges in the boundary. The result is identical failure load to the vertical build 0° specimen without reinforcement. In an additional example, both the 90° horizontal and side build orientation specimens possess hinge reinforcement in the direction of the load. Edge effects cause the response of the 90° side build orientation to be dominated by the influence of hinge reinforcements resulting in a higher tensile load for the 90° side build specimen (24.24 MPa) with respect to the 90° horizontal specimen (15.26 MPa).

The vertical build specimens exhibited the lowest tensile load. The 0° vertical build specimen failed at a higher load than the 90° vertical build specimens indicating stronger adhesion between adjacent layers with longer rasters (i.e., spanning the 13-mm width dimension rather than the 3.5-mm thickness). The ±45° vertical build specimens exhibited the highest ultimate strength among the vertical build specimens, likely due to toughening mechanisms inherent to the ±45° layers.

The results highlighted in this study are fundamental to the development of optimal designs of complex structural materials for lightweight durable components. The application of structural tailoring to AM of complex parts may offer an added benefit via weight reduction and increased structural efficiency. Incorporating the effect of artifacts of FDM processing to enhance strength and failure resistance would significantly enhance a design optimization tool for complex FDM structural components.

Acknowledgements

References

[1] X. Yan, P. Gu, A review of rapid prototyping technologies and systems, Comput. Aided Des. 28 (4) (1996) 307–318.

[2] T. Wohlers, Wohlers Report 2014: Global Reports, Wohlers Associates, Belgium, 2014.

[3] N.W. Choi, M. Cabodi, B. Held, J.P. Gleghorn, L.P. Bonassar, A.D. Strook, Microfluidic scaffolds for tissue engineering, Nat. Mater. 6 (2007) 908–915.

[4] A. Azari, S. Nikzad, The evolution of rapid prototyping in dentistry: a review, Rapid Prototype J. 15 (2009) 216–225.

[5] J.F. Rodrõíguez, J.P. Thomas, J.E. Renaud, Design of fused-deposition ABS components for stiffness and strength, J. Mech. Des. 125 (3) (2003) 545–551.

[6] M.K. Agarwala, V.R. Jamalab, N.A. Langrana, A. Safari, P.J. Whalen, S.C. Danforth, Structural quality of parts processed by fused deposition, Rapid Prototyping J. 2 (4) (1996) 4–19.

[7] J.S. Rovick, An additive fabricator for high speed production of artificial limbs, in: Fifth International Conference on Rapid Prototyping, Dayton, OH, 1994, pp. 47–56.

[8] Y. Feng, T. Siegmund, E. Habtour, J. Riddick, Impact mechanics of topologically interlocked material assemblies, Int. J. Impact Eng. 75 (2015) 140–149.

[9] 3D Printing: Build Your Crazy Robot Ideas at Home, New Scientist, 2823 (2011) 17–18.

[10] http://www.stratasys.com/Products/3D-Printers.aspx.

[11] W. Zhong, F. Li, Z. Zhang, L. Song, Z. Li, Short fiber reinforced composites for fused deposition modeling, Mater. Sci. Eng. A301 (2001) 125–130.

[12] M.L. Shofner, F.J. Rodriques-Macias, R. Vaidyanathan, E.V. Barrera, Single wall nanotube and vapor grown carbon fiber reinforced polymers processed by extrusion freeform fabrication, Compos. Part A 34 (2003) 1207–1217.

[13] E.L. Corral, J. Cesarano III, A. Shyam, E. Lara-Curzio, N. Bell, J. Stuecker, N. Perry, M. Di Prima, Z. Munir, J. Garay, E.V. Barrera, Engineered nanostrucutres for multifunctional single-walled carbon nanotube reinforced silicon nitride nanocomposites, J. Am. Ceram. Soc. 91 (10) (2008) 3129–3137.

[14] A. Bandyopadhyay, R.K. Panda, V.F. Janas, M.K. Agarwala, R. Weeren, S.C. van Danforth, A. Safari, Processing of piezocomposites by fused deposition technique, 10th IEEE International Symposium on Applications of Ferroelectrics 2 (1996) 999–1002.

[15] S.J. Kalita, Development of controlled porosity polymer-ceramic composite scaffolds via fused deposition modeling, Mater. Sci. Eng. C 23 (5) (2003) 611–620.

[16] M. Nikzad, S.H. Masood, I. Sbarski, Thermo-mechanical properties of a highly filled polymeric composites for Fused Deposition Modeling, Mater. Des. 32 (2011) 3448–3456.

[17] D. Espalin, D.W. Muse, E. MacDonald, R.B. Wicker, 3D Printing multifunctionality: structures with electronics, Int. J. Adv. Manuf. Technol. 72 (5–8) (2014) 963–978.

[18] L.R. Holmes Jr., J.C. Riddick, Research summary of an additive manufacturing technology for the fabrication of 3D composites with tailored internal structure, JOM 66 (2) (2014) 270–274.

[19] S.H. Ahn, M. Montero, D. Odell, S. Roundy, P.K. Wright, Anisotropic material properties of fused deposition modeling ABS, Rapid Prototyping J. 8 (4) (2002) 248–257.

[20] K.C. Ang, K.F. Leong, C.K. Chua, Investigation of the mechanical properties and the porosity relationships in fused deposition modelling-fabricated porous structures, Rapid Prototyping J. 12 (2) (2006) 100–105.

[21] V. Vega, J. Clements, T. Lam, A. Abab, N. Fritz, N. Ula, O.S. Es-Said, The effects of layer orientation on the mechanical properties and microstructure of a polymer, J. Mater. Eng. Perform. (2010).

[22] P.M. Pandey, N.V. Reddy, S.G. Dhande, Improvement of surface finish by staircase machining in fused deposition modeling, J. Mater. Process. Technol. 132 (1) (2003) 323–331.

[23] B.H. Lee, J. Abdullah, Z.A. Khan, Optimization of rapid prototyping parameters for production of flexible ABS object, J. Mater. Process. Technol. 169 (2005) 54–61.

[24] E.J. McCullough, V.K. Yadavalli, Surface modification of fused deposition modeling ABS to enable rapid prototyping of biomedical microdevices, J. Mater. Process. Technol. 213 (2013) 947–954.

[25] A.W. Fatimatuzahraa, B. Farahaina, W.A.Y. Yusoff, The effect of employing different raster orientations on the mechanical properties and microstructure of fused deposition modeling parts, IEEE (2011) 22–27.

[26] R.M. Jones, Mechanics of Composite Materials, second edition, Taylor and Francis, Philadelphia, 1999.

[27] ASTM D638-14, Standard Test Method for Tensile Properties of Plastics, ASTM, International, West Conshohocken, PA, 2014.

[28] S.H. Masood, W. Rattanawong, P. Iovenitti, Part build orientations based on volumetric error in fused deposition modelling, Int. J. Adv. Manuf. Technol. 16 (2006) 162–168.

[29] N. Volpato, A. Franzoni, D.C. Luvizon, J.M. Schramm, Identifying the directions of a set of 2D contours for additive manufacturing process planning, Int. J.

Adv. Manuf. Technol. 68 (1–4) (2013) 33–43.

[30] INSIGHT, V9.1, Stratasys, Inc., Eden Prairie, MN.

[31] ASTM D3518/D3518M-13, Standard Test Method for In-Plane Shear Response of Polymer Matrix Composite Materials by Tensile Test of a $\pm45°$ Laminate, ASTM International, West Conshohocken, PA, 2013.